

Final Draft
of the original manuscript:

Agha, N.A.; Liu, Z.; Feyerabend, F.; Willumeit-Roemer, R.; Gasharova, B.;
Heidrich, S.; Mihailova, B.:

**The effect of osteoblasts on the surface oxidation processes of
biodegradable Mg and Mg-Ag alloys studied by synchrotron IR
microspectroscopy.**

In: Materials Science and Engineering C. Vol. 91 (2018) 659 - 668.

First published online by Elsevier: June 06, 2018

DOI: 10.1016/j.msec.2018.06.001

<https://dx.doi.org/10.1016/j.msec.2018.06.001>

The effect of osteoblasts on the surface oxidation processes of biodegradable Mg and Mg-Ag alloys studied by synchrotron IR microspectroscopy

Nezha Ahmad Agha^{1*}, Zhidan Liu^{1*}, Frank Feyerabend^{1**}, Regine Willumeit-Römer¹, Billiana Gasharova², Stefanie Heidrich³, Boriana Mihailova³

¹ Institute of Material Research, Helmholtz-Zentrum Geesthacht, Max-Planck-Str. 1, 21502 Geesthacht, Germany

² Institut für Beschleunigerphysik und Technologie, Karlsruher Institut für Technologie, P.O. Box 3640, Karlsruhe 76021, Germany

³ Department Earth Sciences, University of Hamburg, Grindelallee 48, 20146 Hamburg, Germany

* These authors contributed equally to this study.

**Corresponding author: Frank.Feyerabend@hzg.de

Abstract:

High-resolution analytical methods, including synchrotron infrared microspectroscopy combined with wavelength-dispersive X-ray emission spectroscopy were applied to study the structure and chemical composition of the oxidized layer of pure and Ag-alloyed Mg exposed to cell culture media without and with osteoblasts. Comparative analysis has been done on pure Mg immersed in two different cell culture media: Dulbecco's Modified Eagle's Medium (DMEM) and Roswell Park Memorial Institute medium (RPMI), whereas Mg-xAg binary alloys ($x = 2, 4, 6, 8$ wt. %) were studied after immersion in DMEM. It is shown that the physicochemical formation of degradation products as well as the activity of the biological component is influenced by the addition of silver. It could be demonstrated that the presence of Ag in the Mg alloy enhances the chemical reaction between Mg and C to form amorphous and/or crystalline MgCO₃ on account of CaCO₃. As a consequence, the further available P and Ca react easily to form Mg-poor amorphous calcium phosphate phases. Osteoblasts actively adjusted these phases towards hydroxyapatite-like phases.

Keywords: Mg, degradable bone implants, synchrotron FTIR spectroscopy, EMPA

Introduction

Biodegradable magnesium (Mg) based alloys are considered as a new generation materials of orthopaedic implants, which have the potential to eliminate possible post-surgical complications and can be especially helpful in bone fixation for children. Besides the degradability, magnesium alloys exhibit good mechanical properties comparable to those of bone and good biocompatibility features [1-4]. Additional favourable properties can be induced by selecting smart alloying elements, such as using silver to introduce antibacterial properties. This specific role of silver has been widely investigated and implemented in different biomedical applications [5-7]. For Mg-Ag binary alloy, it has been shown that the addition of silver to a magnesium cast followed by solution heat treatment leads to acceptable levels of degradation and improves the mechanical properties [8]. Therefore, silver is beneficial for functionality as well as for the property profile. Beside the influence of the alloying elements and the material production methods on the alloy microstructure and hence on its degradation [9-13], studies show that magnesium degradation can be influenced by many physiological factors and parameters. This includes the presence of proteins [14, 15], the pH value, the buffering effect of bicarbonate salt in combination with CO₂ [16, 17] as well as other inorganic salts existing in the body fluid [18, 19]. Many in vitro studies are concerned with the influence of magnesium on cells by indirect methods using highly dissolved salts of Mg [20-22]. However, it has been demonstrated that the cell behaviour is better characterized by the use of an extract prepared directly from the real degrading material or even better, by mimicking the in vivo conditions via a direct preparation of cell cultures on the material surface [23]. Yet, there are fewer reports based on such direct methods to study the influence of various types of cells on the chemical composition of the degradation interface [24]. The effect of osteoblasts is particularly important to be understood when studying the transformation of Mg alloys into complex metal oxides. In our former study, the direct interaction between two different binary magnesium alloys (Mg-2wt%Ag and Mg-10wt%Gd) and primary human osteoblasts was investigated for the first time [24]. The emphasis was put on studying the surface morphology and chemical composition via scanning electron microscopy and energy-dispersive X-ray emission spectroscopy (ED-XES). It was demonstrated that the osteoblasts mediate the mineralization process in a different way, depending on the alloying element [24].

Recently, it was demonstrated that normal-incidence infrared reflection (NI IRR) microspectroscopy in combination with wavelength-dispersive X-ray emission spectroscopy (WD-XES) has the great capacity to discriminate the mineral phases developed in the degradation layer to study the developed radial chemical zoning in the oxidized layer [15, 19, 25]. On one hand, WD-XES can quantify the amounts of different chemical elements with much higher precision than ED-XES, while on the other hand, NI IRR can directly detect carbonate and hydrous species, which cannot be quantified by either XES method, and also can distinguish between amorphous and crystalline oxide phases. The lateral resolution of in-house NI IRR microspectroscopy is however restricted to about 50 μm because of the requirement for a relatively flat surface of the probed region to produce a sufficient signal, which is often hampered by the heavy porosity of the degradation layer. The use of synchrotron IR radiation can improve the spatial resolution because the beam can be focused to approximately a 10- μm spot size, which enables better analyses of the heterogeneity of the degradation layer. Besides, the utilization of a synchrotron infrared source ensures acquisition of as high as possible quality of NI IRR spectra. Attenuated total reflection infrared (ATR IR) spectroscopy is another surface sensitive technique used to study micrometer-size spatial areas. Its application is sometimes hindered by the requirement to have a very good contact between the sample surface and the ATR crystal, which may be hardly achievable for heterogeneous materials containing micrometer-sized areas with different hardness. The latter is unfortunately exactly the case of cross sections of corroded metallic rods or disks, comprising multi-zone oxide layer next to the metal inner part. However, ATR IR spectroscopy compares favourably to NI IRR spectroscopy by the fact that the collected ATR IR spectra are only subtly impacted by reflection phenomena and hence, reveal directly the infrared absorption by vibration modes, which makes their interpretation straightforward [26].

The aim of this article is to further extend the study of the effect of osteoblasts on the degradation interface of Mg alloys by analyzing the chemical composition of the corrosion layer via synchrotron infrared microspectroscopy combined with wavelength-dispersive XES. First, we have analyzed pure Mg samples treated without and with osteoblasts in two cell culture media with a different Ca/P ratio, which was previously shown to affect the precipitation of calcium phosphate products [27], to elucidate whether the Ca/P ratio impacts on the osteoblast-induced mineralization processes. Then, we have studied different Mg-xAg binary alloys ($x = 2, 4, 6, 8$ wt. %) exposed to

the same cell culture medium without and with osteoblasts, to check to which extent the presence of silver changes the effect of osteoblasts .

2. Materials and Methods

2.1. Samples

Raw materials, magnesium 99.99 wt.% (Xinxiang Jiuli Magnesium Co., Ltd, Xinxiang, China) and silver granules (99.99 wt.%, ESG Edelmetall-Handel GmbH. & Co. KG, Rheinstetten, Germany) were applied for the preparation of Mg-xAg alloys with x = 2, 4, 6, and 8 wt%. Pieces of high purity magnesium were put into a steel crucible together with the corresponding amount of silver. Melting was done at 750°C with protection of 98 % argon (Ar) and 2 % sulphur hexafluoride (SF₆), and then stirred at 200 rpm for half an hour. After the temperature decreased to 730°C, the melt was transferred into a permanent steel mould. The mould was held for 15 min at 680°C under protective atmosphere and chilled in flowing room-temperature water directly at a speed of 100 cm/min. The high purity magnesium ingots were recast following the same solidification procedures. Table 1 shows the chemical composition determined by spark emission spectrometry (Spectrolab M, Spektro, Kleve Germany) for Mg, iron (Fe), copper (Cu), and nickel (Ni), and the concentration of Ag determined by X-ray fluorescence spectrometry (Bruker AXS S4 Explorer, Bruker AXS GmbH, Karlsruhe, Germany). Heat treatment was performed in a resistance furnace (Linn Elektro Therm AK 40. 06, Bad Frankenhausen, Germany) at 430°C for at least 6 hours followed by quenching in water at room temperature. For extrusion, the ingots were heated up to 300°C and processed by hot extrusion (Strangpresszentrum Berlin, Berlin, Germany) in which the extrusion ratio and stamp advance rate were 108 and 0.7 mm/s, respectively.

Discs with diameter of 10 mm and thickness of 1.5 mm were machined from the extruded bars (Henschel KG, Munich, Germany). The samples were subsequently sterilized using gamma radiation at a dose of 29.2 KGy (BBF Sterilisationservice GmbH, Kernen, Germany).

Table. 1. Chemical composition and impurity levels of the studied alloys.

Alloy	Chemical composition wt. %				
	Ag	Fe	Cu	Ni	Mg
Pure Mg	-	0.0042	0.0021	0.0006	Bal.
Mg-2Ag	2.4	0.0048	0.0017	0.0007	Bal.

Mg-4Ag	4.4	0.0028	0.0014	0.0011	Bal.
Mg-6Ag	6.3	0.0021	0.0010	0.0011	Bal.
Mg-8Ag	8.5	0.0018	0.0010	0.0011	Bal.

2.2 Immersion procedure

Pure-Mg samples were immersed in two different basic corrosion media: Dulbecco's Modified Eagle's Medium (DMEM; Life technologies, Darmstadt, Germany) and Roswell Park Memorial Institute medium (RPMI-1640; Sigma-Aldrich, Taufkirchen, Germany) containing 10 % Fetal Bovine Serum (FBS; PAA laboratories, Linz, Austria) and 1 % Penicillin/Streptomycin (P/S; Invitrogen, Darmstadt, Germany). The Ca/P ratio of DMEM-based and RPMI-based corrosion medium was 2 and 0.07 respectively (Table 2). The Mg-xAg alloys (x = 2, 4, 6, 8 wt %) were treated only in DMEM-based corrosion media. The immersion was performed resembling the procedure described in details in [24]. First, the samples were pre-incubated for 24 h under cell culture conditions (37°C, 20% O₂, 5% CO₂, 95% relative humidity). Then, the medium was removed and 100 000 human primary osteoblasts were cultured in 50 µL medium on the surface and allowed to adhere for 30 min in the incubator (Heraeus BBD 6620, Langenselbold, Germany). After that, 3 mL medium was added to continue the immersion under cell culture conditions for up to 14 days [24, 28], with a complete medium exchange every 2-3 days. Primary human osteoblasts were isolated according to the Declaration of Helsinki as previously described [29]. For each material treatment control samples without osteoblasts were also prepared by the same protocol (see Table 3).

~~Table 2. Concentration of inorganic salts in the used cell culture media.~~

Concentration [mM]	DMEM Glutamax	RPMI-1640
Bicarbonate	44.1	23.8
Calcium	1.8	0.4
Chloride	117.5	108.0
Magnesium	0.81	0.4
Potassium	5.3	5.4
Phosphate	0.9	5.6
Sulphur	0.8	0.4
Sodium	155.3	137.0

Table 3. Sample nomenclature and treatment conditions. (C) refers to control samples and (O) to samples treated with osteoblasts. Immersion time was 14 days for all samples after 1 day preincubation.

Sample	Metal	Basic medium	Osteoblasts
Mg _{RPMI} -C	Mg	RPMI + 10% FBS + 1% P/S	No
Mg _{RPMI} -O	Mg	RPMI + 10% FBS + 1% P/S	Yes
Mg _{DMEM} -C	Mg	DMEM + 10% FBS + 1% P/S	No
Mg _{DMEM} -O	Mg	DMEM + 10% FBS + 1% P/S	Yes
MgAg2-c	Mg-2Ag	DMEM + 10% FBS + 1% P/S	No
MgAg2-o	Mg-2Ag	DMEM + 10% FBS + 1% P/S	Yes
MgAg4-c	Mg-4Ag	DMEM + 10% FBS + 1% P/S	No
MgAg4-o	Mg-4Ag	DMEM + 10% FBS + 1% P/S	Yes
MgAg6-c	Mg-6Ag	DMEM + 10% FBS + 1% P/S	No
MgAg6-o	Mg-6Ag	DMEM + 10% FBS + 1% P/S	Yes
MgAg8-c	Mg-8Ag	DMEM + 10% FBS + 1% P/S	No
MgAg8-o	Mg-8Ag	DMEM + 10% FBS + 1% P/S	Yes

2.3. Sample preparation for spectroscopic analyses

In order to study the structural and chemical changes across the degraded surface layer by infrared microspectroscopy and wavelength-dispersive electron-induced x-ray emission spectroscopy, the treated disks were cut in half using a precision diamond wire saw (Well Walter Ebner, Le Locle, Switzerland). One half of each dry sample was then embedded in resin (Reckli Injektionsharz, Reckli GmbH, Herne, Germany) with the cross section oriented upwards and subsequently polished with 0.1- μ m colloidal silica suspension at the final stage of fine polishing. The other half was used for the analysis by micro X-ray fluorescence spectroscopy. Such a sample handling excludes the possibility of artificially induced mechanical cracks and post-treatment chemical changes in the examined area. The only plausible contamination may come from the aggregates of amorphous silica nanoparticles used for final polishing in cavities in the degradation layer, which, if any, are well distinguishable from the degradation products by both spectroscopic methods.

2.4. Degradation rate by the mass loss method

The degradation rate of pure Mg upon different treatment conditions was determined based on the mass loss after 14 days of immersion, whereas that of Mg-2Ag alloys after 7 days of immersion. Before sample sterilization, the initial weight of the samples was recorded. Six samples were immersed in 2 mL of immersion medium. The immersion medium was changed every 3-4 days to facilitate a semi-static immersion test and prevent saturation effects. After immersion, the subsequently formed products were removed by treating the corroded disk with chromic acid (180 g/L in distilled water, VWR international, Darmstadt, Germany) for 20 min at room temperature. The degradation rate (DR) was calculated in mm/year using the following equation:

$$DR = \frac{8.76 \times 10^4 \times \Delta g}{A \times t \times \rho} \quad (1)$$

where Δg is the mass change in grams, A is the initial surface area of the sample in cm^2 , t is the immersion time in hours, and ρ is the alloy density in g/cm^3 .

2.5. pH measurements of the treatment solution

The pH was measured continuously throughout the immersion period using the SDR SensorDish reader system (PreSens GmbH, Regensburg, Germany). Special 24-well plates were used with an integrated pH sensor (HydroDish, PreSens GmbH, Regensburg, Germany). The measurement method is based on a non-invasive luminescence detection. The detectable pH values in this system ranged from pH 5 to 9. The experiments were performed by incubating 6 samples of each group (each alloys, with and without cells) in 2 mL of the immersion medium for 14 days. During the immersion and prior to the medium exchanges, the pH values of the supernatants were measured after shaking (pH-meter Titan X, Fisher Scientific GmbH, Schwerte, Germany) to compare values and ensure the validity of the online pH measurement.

2.6. Cell viability by LIVE/DEAD (Viability/Cytotoxicity) staining assay

The cell coverage and viability were assessed using a LIVE/DEAD (Life Technologies, Darmstadt, Germany) assay after 14 days of immersion. The staining solution was prepared by adding 4 μL Calcein AM (LIVE) and 10 μL Ethidium homodimer-1 (DEAD) to 10 mL of phosphate buffered saline (PBS). The samples were washed with PBS to eliminate the non-adherent cells and staining solution was added (1.5 mL / sample) under cell culture conditions for 20 minutes. The staining solution was then replaced with DMEM, and the samples were visualized by fluorescent microscopy (Nikon, eclipse

Ti, Düsseldorf, Germany). The following filters were used: Fluorescein Isothiocyanate; FITC (Ex: 465-495 nm; Em: 515-555 nm; Mirror at 505 nm), and Texas red (Ex: 540-580 nm; Em: 600-660; Mirror at 595 nm).

2.7. Powder X-ray diffraction

All treated samples were subjected to powder X-ray diffraction (XRD) in reflection mode to check whether crystalline phases were formed in the oxidized layer. The XRD patterns were collected with Stoe Stadi-MP powder X-ray diffractometer (Stoe & Cie GmbH, Darmstadt, Germany) using a position sensitive detector (PSD) and monochromatized Cu K_{α} radiation $\lambda = 1.5406$ nm. XRD data were measured in the 2θ range $5^{\circ} - 50^{\circ}$, with a 2θ step size of 0.005° , a PSD step of 1.5° , and an accumulation time of 240 s per PSD step.

2.8. Electron-induced X-ray emission spectroscopy

Backscattered electron (BSE) imaging, chemical element mapping, and electron microprobe analysis on the cross sections of corroded discs was performed with a Cameca Microbeam SX100 SEM-system using a wavelength-dispersive detector (Cameca, Gennevilliers Cedex, France). The energy of the electron beam was 15 keV and the beam current was 20 nA. The mapping was conducted for carbon (C), nitrogen (N), oxygen (O), sodium (Na), calcium (Ca), phosphorus (P), sulphur (S), chlorine (Cl), and potassium (K) with a lateral spatial size of $0.1 \mu\text{m}$ and a detection limit in the range of 100-300 ppm. Electron microprobe analysis (EMPA) to quantify the content of oxides in wt% was attempted in at least 25 points from each sample, as the probed areas were visually free of micro-cracks and cavities. The achieved lateral resolution was $\sim 1 \mu\text{m}$. The standards used were albite for Na, MgO for Mg, apatite for P, BaSO_4 for S, vanadinite for Cl, orthoclase for K, and andradite for Ca. The carbon content could not be quantitatively determined by this method because of the necessity to coat the sample surface with a conductive layer of carbon.

2.9. Synchrotron Fourier Transform infrared (FTIR) microspectroscopy

Synchrotron-based FTIR spectroscopic experiments were conducted at the Infrared/THz microspectroscopy beamline IR2 of the 2.5-GeV synchrotron facility ANKA, Karlsruhe. The spectra were measured with a Bruker Vertex 80v spectrometer coupled to a Bruker IRscope II microscope equipped with a liquid- N_2 -cooled MCT detector (InfraRed Associates Inc., Stuart, FL) and a KBr beam splitter (Bruker Optik GmbH,

Ettlingen, Germany). The microscope was sealed in a home-made N₂-purged compartment to ensure a humidity level during the measurements less than 3%. NI IRR spectra were collected in the range of 600-5000 cm⁻¹ with a 36× infrared objective. The area sensed by the detector was varied between 9 and 18 μm, depending on the size of the sample region from which the spectra were collected. A background spectrum was collected from a clean Au surface. In some cases, to verify the interpretation of NI IRR spectra, complementary ATR IR spectroscopy was applied. The ATR IR spectra were collected with an ATR 20× objective with a Ge crystal having a 45° inclination angle to the incoming beam. The lateral resolution of the ATR IR spectra, determined from the aperture used, was 11 μm. The background spectrum was collected in air. The spectra measured by both the NI IRR and ATR methods were averaged over 512 scans, using instrumental resolution of 2 cm⁻¹; the background spectrum was always measured just before measuring each sample spectrum in order to eliminate the influence of the decay of the synchrotron electron beam current on the signal. For each sample, spectra from at least four different points were collected.

2.10 Micro X-ray fluorescence spectroscopy (μ-XRF)

In order to analyse the elemental composition of the degradation layer, μXRF measurements were performed on the surface of the Mg-Ag samples. Element analysis of the degraded surface (an area of 5 x 2 mm) was performed with a Tornado M4 (Bruker nano, Berlin, Germany). The X-ray spectrometer was equipped with a Rh tube working at a voltage of 50 kV and an anode current of 600 μA and operated under vacuum conditions (20 mbar). The material was mapped with a spot size of 25 μm, a spot distance of 10 μm and an acquisition time of 1 ms pixel⁻¹. Analyte element selection was done according to multipoint measurement and Mg, Ag, Ca, P, and S were chosen. Data evaluation and image processing were done with the Bruker ESPRIT software (version 1.3.0.3273).

Results and Discussion

Degradation behaviour

The degradation rate was measured after 14 days of immersion using the mass loss method (see Figure 1). The results show that the degradation rate values for pure Mg samples treated in RPMI and DMEM without cells are comparable. However a slight difference in the presence of osteoblast cells was recorded, as the cells slightly reduced

the degradation rate in the case of DMEM, while the opposite effect was observed for RPMI. The cell effect is negligibly small for Mg-2Ag treated in DMEM. The other silver containing alloys showed the same trend (data not shown). The results regarding the degradation rate are in accordance with the measured pH values, which are higher after the first 72 h of immersion in presence of cells for pure Mg immersed in RPMI (see Fig. 2a), but lower for pure Mg immersed in DMEM (Fig. 2b) and Mg-2Ag in DMEM. The trends in the pH values for Mg-2Ag treated in DMEM are similar to that of pure Mg (see Figs 2b and 2c). Interestingly, after 300 h of immersion the effect of the cells on the pH values is reversed for both Mg-xAg alloys and pure Mg, indicating that a prolonged treatment in the presence of osteoblasts leads to a decrease in the pH value in the case of DMEM and an increase in the case of RPMI. The strong dependence of the effect of osteoblasts on the basic culture medium emphasizes the importance of the ratio between bicarbonate and phosphate constituents in the immersing solution (see Table 1) on the oxidation kinetics.

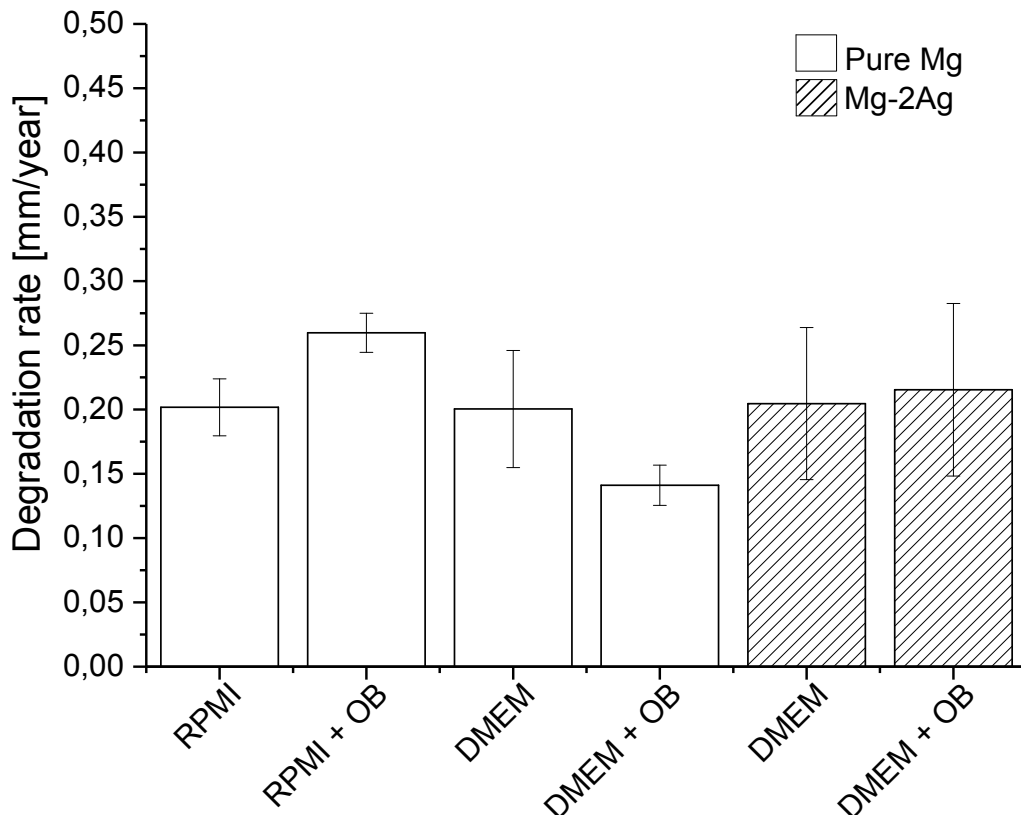


Figure 1: Mean degradation rate [mm/year] according to the weight loss method for pure Mg immersed in RPMI and DMEM, and Mg-2Ag immersed in DMEM.

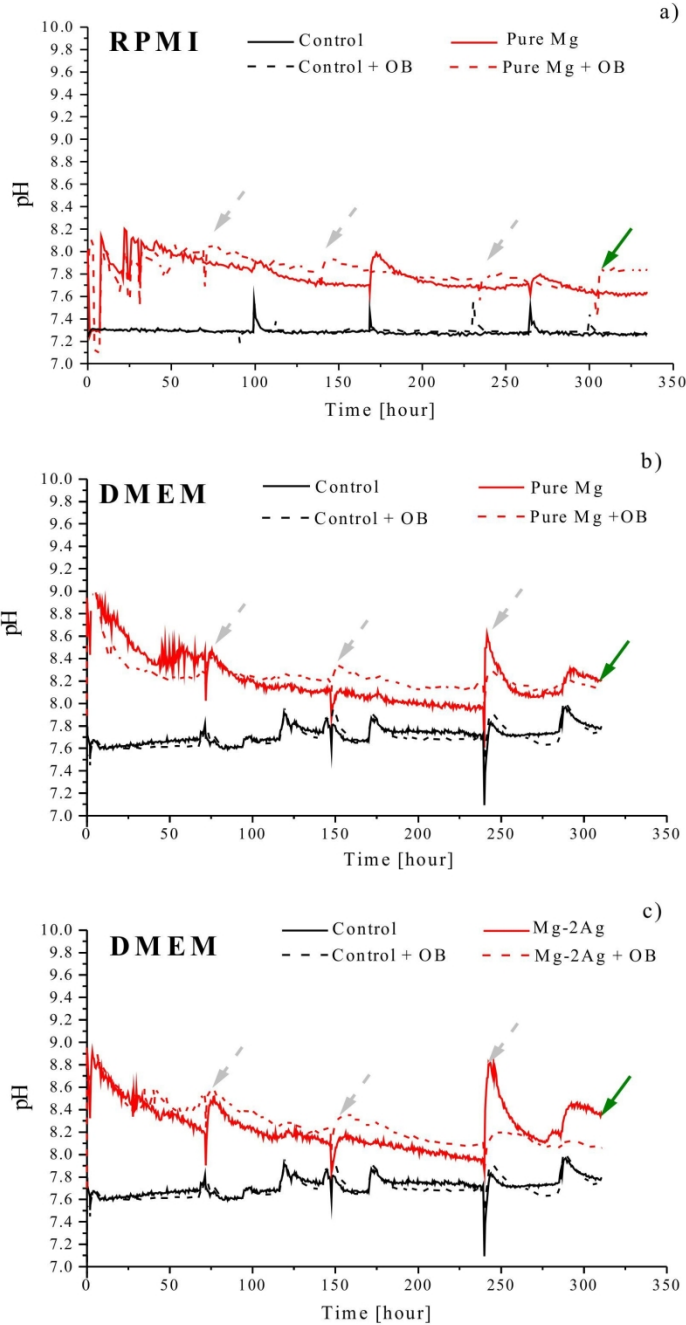


Figure 2: Online pH measurements during 14 days of immersion. A): pure Mg samples immersed in RPMI, B): pure Mg samples immersed in DMEM and C): Mg-2Ag immersed in DMEM. Controls were measured on tissue culture plates. Arrows in gray refer to the medium exchange and in green to the end point of immersion.

Live/Dead staining

Cell viability was determined by Live/Dead staining to make sure, that the analysed effects are evoked by the presence of osteoblasts on the material surface. As can be seen in Fig. 3, the cells were mostly healthy after 14 days of immersion, showing good development and distribution in the different conditions.

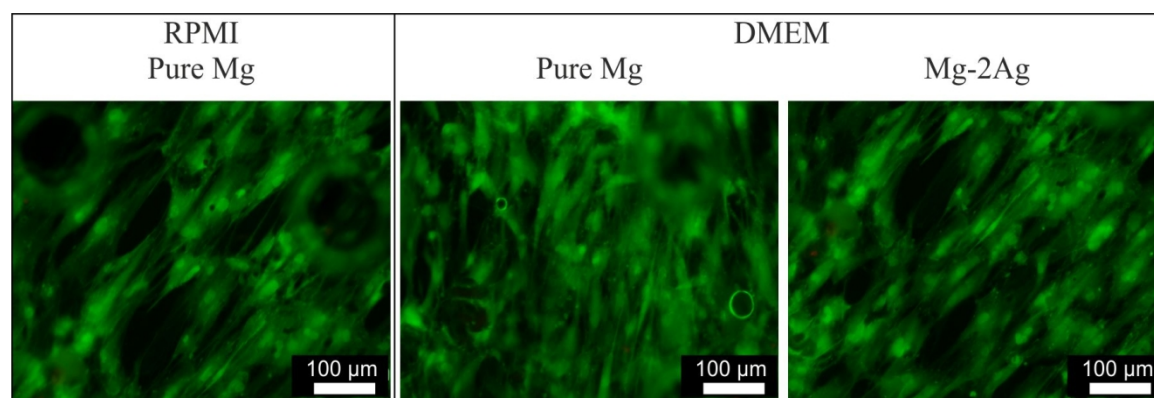


Figure 3: Fluorescence images of osteoblasts cultured on metallic disks after 14 days of immersion in the corresponding cell culture medium.

Phase composition of the oxidized layer

According to powder XRD analysis, the oxidized layers of all samples studied here are amorphous.

Pure-Mg samples

Figure 4 shows typical NI-IRR spectra of the corroded layer for pure Mg samples immersed in RPMI or DMEM, without and with osteoblasts. Two main bands are observed for all samples: near 1000 cm^{-1} related to PO_4 stretching and near 1400 cm^{-1} due to the CO_3 stretching. The absence of a second, longitudinal optic component in

either band confirms that the formed oxides are non-crystalline [15]. The intensity ratio between the two bands reveals that the phosphate phase is dominant over the carbonate phase for both samples treated with RMPI as well as for pure Mg exposed to DMEM without osteoblasts. In the case of DMEM, the presence of osteoblasts reverses the ratio between the phosphate and carbonate phases. The IR spectroscopic results are in good agreement with the EMPA data (see Table 4). The latter also reveal that phosphate is the dominant oxide in the corroded layer of $Mg_{\text{RMPI-C}}$, $Mg_{\text{RMPI-O}}$ and $Mg_{\text{DMEM-C}}$, while it is minor for $Mg_{\text{DMEM-O}}$. It should be however strongly emphasized that the ratio between the content of CaO and P_2O_5 for $Mg_{\text{RMPI-C}}$, $Mg_{\text{RMPI-O}}$ and $Mg_{\text{DMEM-C}}$ is far lower than that of hydroxyapatite (compare the data in Tables 4 and 5). Therefore, the formed amorphous phosphate phase is not chemically related with the desired apatite-like phase. The chemical element mappings (Fig. 5) also did not show a clear spatial correlation between P and Ca, suggesting that the amorphous phosphate phase is a mixed magnesium-calcium phosphate. The ratio CaO : P_2O_5 for $Mg_{\text{DMEM-O}}$ is higher than compared to the other three pure Mg samples, but it matches better the nominal ratio of dicalcium phosphate $CaHPO_4$ rather than that of hydroxyapatite. The PO_4 peak position in the NI IRR spectrum of $Mg_{\text{DMEM-O}}$ differs from that in the NI IRR spectra of $Mg_{\text{RMPI-C}}$, $Mg_{\text{RMPI-O}}$ and $Mg_{\text{DMEM-C}}$, which also indicates the formation of chemically different amorphous phosphate phase in the case of exposure to DMEM with osteoblasts.

The NI IRR spectra collected from $Mg_{\text{RMPI-O}}$ show an additional sharp feature near 1280 cm^{-1} , which is close to the vibration of double P=O bond in infrared absorption spectra [30, 31]. To verify the origin of this peak and to shed light on the amorphous phosphate phases, the samples were further subjected to ATR IR spectroscopy. Selected spectra ATR IR spectra are shown in Fig. 6. A sharp peak in the range $1250 - 1260\text{ cm}^{-1}$ was indeed detected via ATR IR spectroscopy, including in some areas of samples $Mg_{\text{RMPI-C}}$ and $Mg_{\text{DMEM-O}}$, which unambiguously indicates the formation of P=O functional groups. Evidences for presence of P=O bonds were not found only in the oxidized layer of $Mg_{\text{DMEM-C}}$. This, along with the fact that P=O bonds are abundant in $Mg_{\text{RMPI-O}}$ as revealed by NI IRR, implies that osteoblasts enhance the formation of P=O functional groups, independently of the basic cell culture medium. It is worth noting that in the absence of osteoblasts the two degradation media result in the formation of different phase zonation and in particular different amorphous phosphate phases (see Fig. 6). The comparison between the ATR IR spectra of $Mg_{\text{RMPI-C}}$ and $Mg_{\text{DMEM-C}}$ show that the

oxidized layer of pure Mg exposed to RPMI exhibits areas rich of P=O as well as areas rich of a non-crystalline phosphate phase containing considerably amount of NH₄ and hydrous species (H₂O, OH⁻). In contrast, the oxidized layer of pure Mg exposed to DMEM comprises a narrow inner zone rich of amides and a thicker outer zone of metal phosphate poor of hydrous and ammonium species.

Early bone mineral formation is a highly disputed process. Three redundant calcification mechanisms are thought to play a pivotal role: (I) ion-based nucleation models, where charged proteins associated with collagen induce mineral nucleation via ions in solution independent of cell presence [32]; (II) Matrix vesicle induced accumulation of calcium and phosphate and subsequent rupture of the formed crystals, which is a cell-dependent process [33]; and (III) transient amorphous calcium phosphate (ACP) formation, which has recently been shown to be mediated by complex intracellular transport mechanisms of osteoblasts [34, 35]. All these pathways are dependent on the secretion of collagen by osteoblasts. In our study it was shown that the formation of ACP (in the form of mixed Mg/Ca-phosphates) can also occur via a material induced cell independent pathway (Fig. 4, Mg_{RPMI-C} and Mg_{DMEM-C}). This acellular formation can be hypothesized to facilitate and accelerate bone formation, as it is observed also in *in vivo* experiments [36, 37].

Since the concentration of phosphorous, magnesium and calcium in DMEM Glutamax is closer to that in whole blood [25] than the corresponding inorganic constituents in RPMI (see Table 2), the Mg-Ag alloy samples were treated in DMEM, to follow the effect of Ag on the degradation processes without and with osteoblasts. Moreover, cell cultivation of osteoblasts in RPMI was shown to have a partly inhibitive effect on osteoblast differentiation [38].

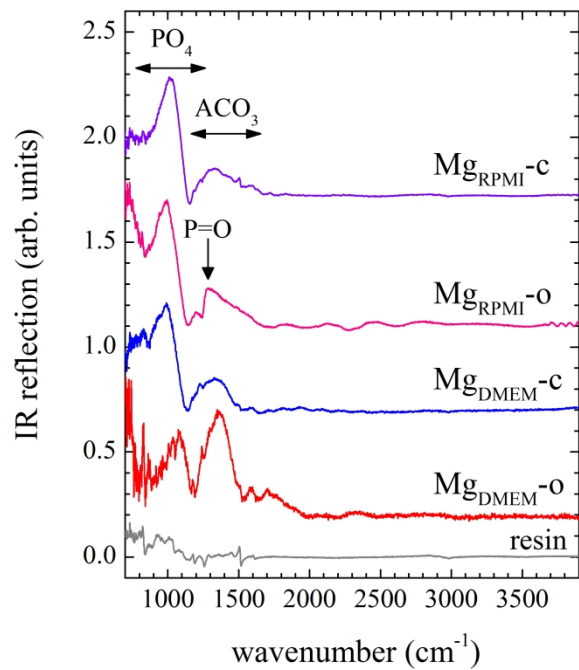


Figure 4: Representative NI IRR spectra of degraded pure-Mg samples; the spectrum of the resin in which the cross-section cuts were embedded is also shown to facilitate the identification of artificial signals, if any. The spectra are vertically offset for clarity.

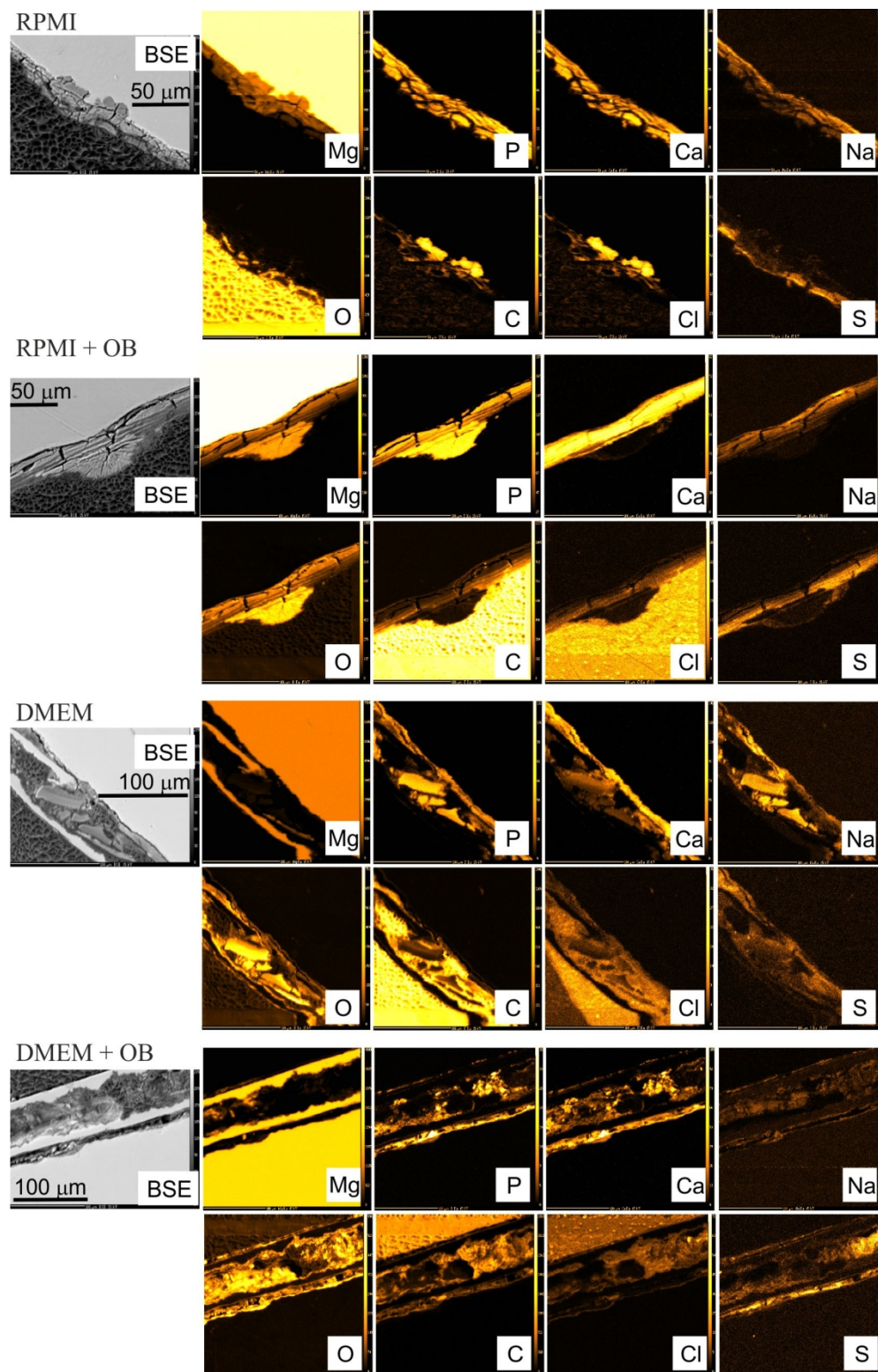


Figure 5: Backscattering electron (BSE) images and selected chemical element mappings of $\text{Mg}_{\text{RPMI-C}}$, $\text{Mg}_{\text{RPMI-O}}$, $\text{Mg}_{\text{DMEM-C}}$, and $\text{Mg}_{\text{DMEM-O}}$.

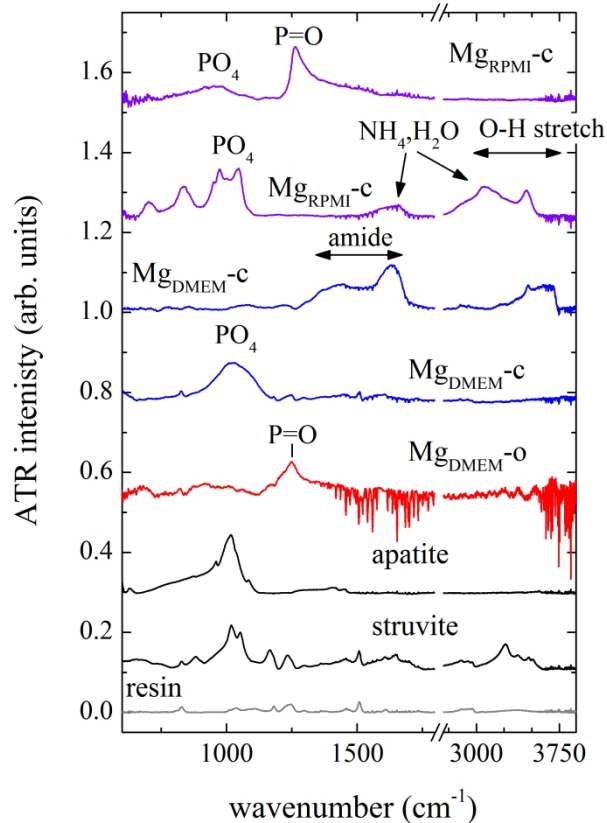


Figure 6: Selected ATR IR spectra of degraded pure-Mg samples, along with reference spectra of apatite $\text{Ca}_5(\text{PO}_4)_3(\text{OH}, \text{F}, \text{CO}_3)$ and struvite $\text{NH}_4\text{MgPO}_4 \cdot 6\text{H}_2\text{O}$ as well as of the resin in which the samples were embedded. Spectra measured from different areas of the same sample are displayed for $\text{Mg}_{\text{RPMI-c}}$ and $\text{Mg}_{\text{DMEM-c}}$; peak assignment according to [30]. The spectra are vertically offset for clarity.

Mg-Ag samples

Representative NI IRR spectra of Mg-Ag disks immersed in DMEM without and with osteoblasts are shown in Fig.7. As can be seen, the addition of Ag to the metal alloy promotes the formation of ACO_3 , on the account of phosphate phases. The ATR IR spectra (not shown) and EMPA data (Table 4) confirms the dominance of carbonate in the oxidized layer. Furthermore, the chemical-element mappings (see for example Fig. 8) indicate that the spatial distribution of P correlates with that of Ca, which implies that the formed carbonate phase is MgCO_3 . Indeed the amount of measured total oxide wt% in zones which are poor of P_2O_5 (see Table 4, e.g. MgAg6-c , MgAg8-c , MgAg8-o) matches within uncertainties the expected value of 47.8 wt% for magnesite (see Table 5). Most of the samples possess an outermost rim, the NI IRR spectrum of which

contains both the longitudinal optic and transverse optic components of CO_3 stretching (see Fig. 7), indicating the presence of incipient crystalline magnesite [15].

Thus the combined analyses clearly demonstrate that the presence of Ag in the Mg alloy enhances the chemical reaction between Mg and C to form amorphous and/or crystalline MgCO_3 on account of CaCO_3 . As a consequence, the further available P and Ca react easily to form Mg-poor amorphous calcium phosphate phases. Furthermore, MgCO_3 has a higher catalytic activity than the bulk metal [39] and therefore can influence the degradation rate.

The examination of CaO-to- P_2O_5 ratio of oxidized layer of Mg-Ag samples (see Table 4) provides another quite interesting result: the presence of osteoblast in the cell culture medium changes the chemistry of the calcium phosphate phases in a way to become closer to the CaO : P_2O_5 ratio of hydroxyapatite (see Table 5). The effect is particularly pronounced for MgAg6-o and MgAg8-o, which exhibit areas with CaO : P_2O_5 ratio ~1.3 – 1.4, matching very well the calculated value of 1.32 for hydroxyapatite. Therefore also the relative element abundance in the degradation layer was analysed by μXRF (see Figure 9). Here several effects of osteoblast could be observed: (I) in the presence of osteoblasts the formation and ratio of Ca:P was in all cases increased in the presence of osteoblasts compared to the control; (II) starting from Mg-4Ag an accumulation of silver in the degradation layer can be observed, which is lower in the presence of osteoblasts.

Taking all the results together, two mechanisms are responsible for the increase of calcium phosphates on magnesium-silver alloys:

1. The acellular chemical formation of calcium carbonates, presumably following the reaction route vaterite – aragonite – calcite [40, 41], followed by chemical transformation to amorphous calcium phosphates [42] and magnesite, and
2. osteoblasts act as a structure-directing agent, adjusting the chemical composition in the amorphous calcium carbonate / calcium phosphate phase to resemble that of bone mineral component and secreting their own matrix.

Further studies should elucidate, whether the degradation environment in the vicinity of magnesium alloys can have a direct influence on the above mentioned calcification pathways.

Finally, from an alloy point of view, the major part of the oxidation layer of MgAg6-o seems to be relatively homogenous, according to both IR microspectroscopy and EMPA, containing approximately 71% of amorphous MgCO_3 and 22% amorphous calcium phosphate with composition corresponding to hydroxyapatite. This suggests that a Mg-Ag alloy of 6 wt% is quite suitable for biodegradable implants from the point of view of phase composition.

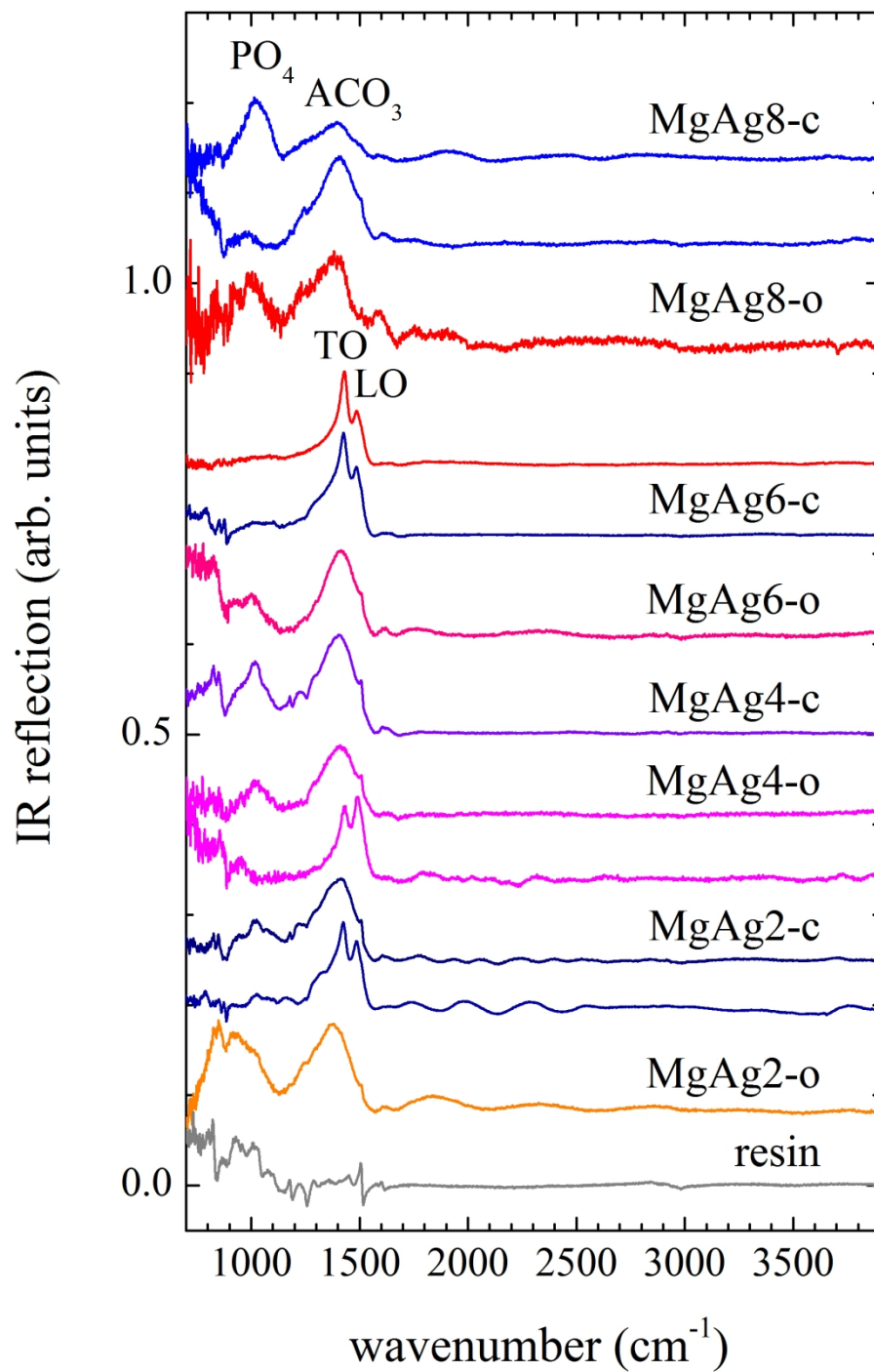


Figure 7: Typical NI IRR spectra of degraded Mg-Ag samples; the spectrum of the resin in which the samples were embedded is also shown to facilitate the identification of artificial signals, if any. LO and TO stand for longitudinal optic and transverse optic, respectively. The spectra are vertically offset for clarity

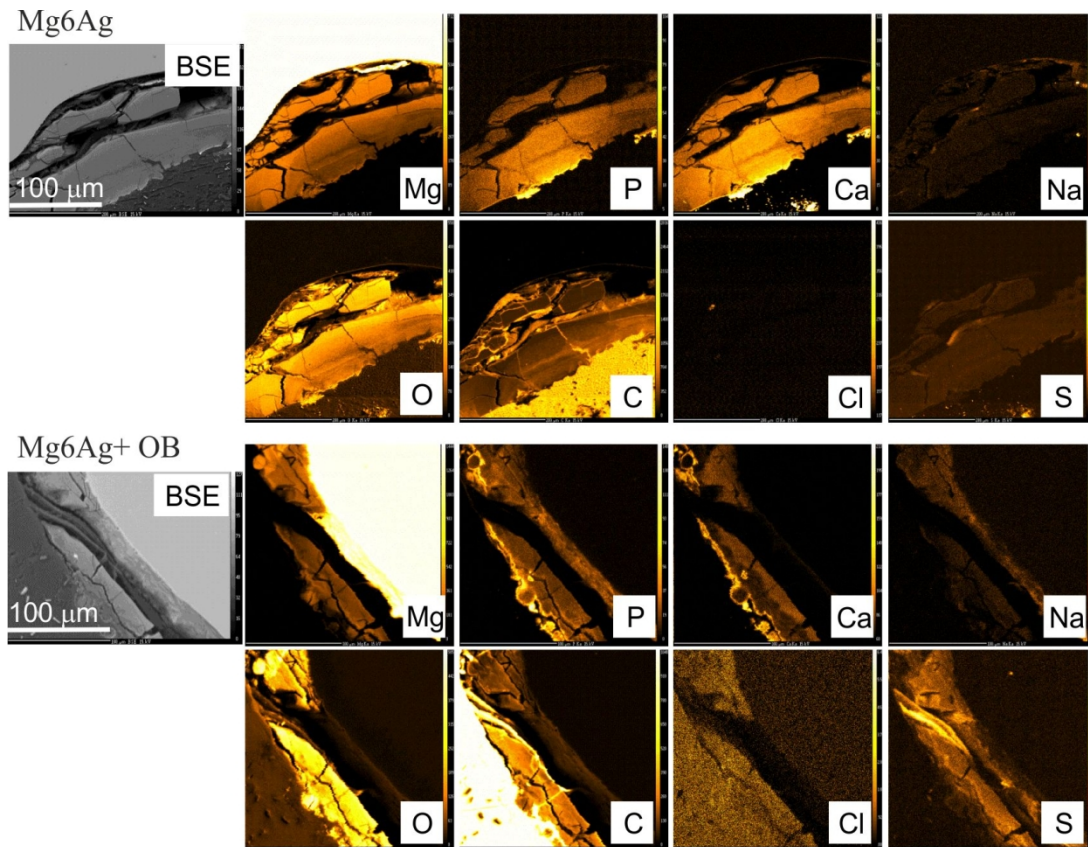


Figure 8: Backscattering electron (BSE) images and selected chemical element mappings of MgAg6-c and MgAg6-o. The rest of Mg-xAg samples show similar trends.

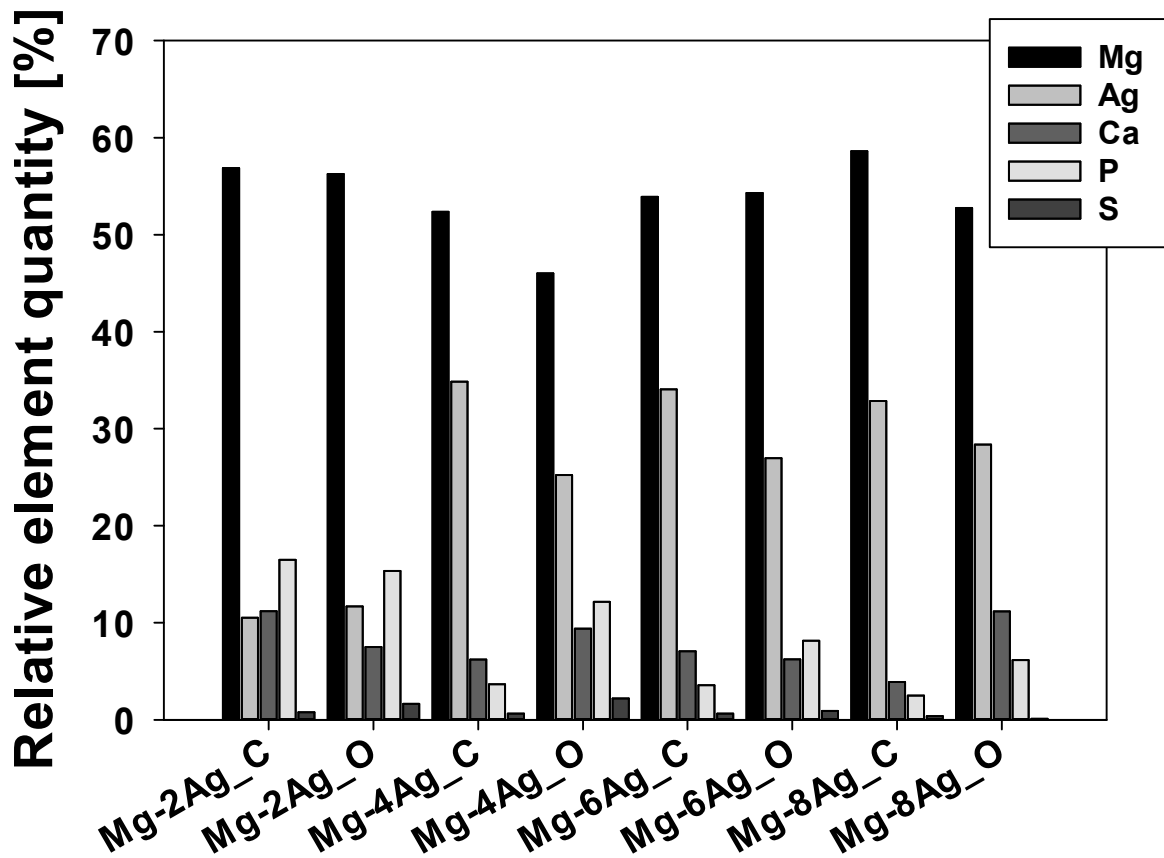


Figure 9: μ XRF analysis of the relative element abundance in the degradation layer. Given are the alloys and the absence (C) and presence (O) of human osteoblast cells.

Table 4: Mean contents of the main oxides (wt%) and chlorine measured in the degradation layer. Total oxides strongly deviate from the typical value from 99-101% due primarily to the presence of light elements such as H and C; porosity of the oxidized layer may further lower the total oxide values. Multiple values are given in the case of apparent chemical zonation.

	MgO	P ₂ O ₅	CaO	Na ₂ O	K ₂ O	SO ₂	Cl	CaO : P ₂ O ₅	Total oxide
Mg _{RPMI} -c	19±9	25±4	12.3±0.7	1.0±0.3	0.14±0.03	0.4±0.1	0.33±0.05	~0.5	57±3
Mg _{RPMI} -o	16±1	32±1	14.9±0.5	0.60±0.03	0.07±0.01	0.43±0.05	0.20±0.01	~0.5	67±2
Mg _{DMEM} -c	28±6	29±8	5±2	1.3±0.6	0.21±0.05	0.22±0.08	0.11±0.06	~0.2	64±5
	18±8	20±6	8±2	0.4±0.1	0.08±0.03	0.4±0.1	0.20±0.04	~0.4	47±1
Mg _{DMEM} -o	28±10	4±2	3±1	0.2±0.1	0.05±0.03	0.13±0.07	0.40±0.02	~0.75	36±5
MgAg2-c	24±3	1.8±0.5	3.4±0.8	0.23±0.06	0.05±0.01	0.17±0.05	0.29±0.03	~1.9	30±3
MgAg2-o	29±4	4.4±0.8	5±1	0.27±0.05	0.06±0.01	0.6±0.1	0.15±0.02	~1.1	40±5
MgAg4-c	23±3	3.5±0.4	3.7±0.9	0.30±0.05	0.03±0.01	0.6±0.3	0.5±0.2	~1.0	32±3
MgAg4-o	26±4	4.4±0.2	4.2±0.3	0.26±0.04	0.04±0.01	0.77±0.06	0.20±0.01	~0.95	36±4
MgAg6-c	20±4	8±2	5±1	0.21±0.02	0.02±0.01	0.9±0.1	0.28±0.01	~0.63	34±2
	46±4	0.4±0.2	0.8±0.1	0.11±0.03	0.01±0.01	0.3±0.1	0.06±0.04	~2	47±4
MgAg6-o	27±3	3.7±0.9	4.7±0.7	0.33±0.07	0.03±0.01	1.0±0.4	0.20±0.05	~1.3	38±1
MgAg8-c	18±3	6±1	5.0±0.8	0.38±0.09	0.03±0.02	0.9±0.1	0.42±0.05	~0.8	31±4
	42±3	0.4±0.3	0.80±0.08	0.08±0.04	0.01±0.01	0.2±0.1	0.05±0.02	~2	44±3
MgAg8-o	24±3	5±1	4.5±0.1	0.27±0.03	0.04±0.01	0.80±0.06	0.15±0.03	~0.9	34±4
	43±7	1.1±0.3	1.5±0.3	0.18±0.08	0.05±0.02	0.2±0.1	0.05±0.03	~1.4	47±7

Table 5: Theoretical oxide values in wt% for reference oxide compounds that can be formed under culture cell conditions simulating those in a human body.

Reference compounds	MgO	P ₂ O ₅	CaO	CaO : P ₂ O ₅	Total oxide
MgCO ₃ (magnesite)	47.8				47.8
Mg(OH) ₂ (brucite)	69.1				69.1
Ca ₅ (PO ₄) ₃ OH (hydroxyapatite)		42.4	55.8	1.32	98.2
Ca(H ₂ PO ₄) ₂ (monocalcium phosphate)		60.7	23.9	0.39	84.6
CaHPO ₄ (dicalcium phosphate)		52.2	41.2	0.79	93.4
Ca ₈ H ₂ (PO ₄) ₆ ·5H ₂ O (octacalcium phosphate)		43.4	45.6	1.05	89
Mg ₅ (PO ₄) ₃ OH	47.6	50.3			97.9
Mg(H ₂ PO ₄) ₂	18.5	65.0			83.5
MgHPO ₄	33.5	59			92.5
Mg ₈ H ₂ (PO ₄) ₆ ·5H ₂ O	37.7	49.7			87.4
CaC ₂ O ₄ ·H ₂ O (whewellite)	38.4				38.4
CaC ₂ O ₄ ·2H ₂ O (weddellite)	34.2				34.2
MgC ₂ O ₄ ·H ₂ O (Mg oxalate)		30.9			30.9
MgC ₂ O ₄ ·2H ₂ O (glushinskite)		27.2			27.2
NH ₄ CaPO ₄ ·6H ₂ O		28.9	19.5	0.67	44.2
NH ₄ MgPO ₄ ·6H ₂ O (struvite)	16.4	24.7			45.3

Conclusions

Two general conclusions can be gained from the analyses of the phase composition of the degradation layers of Mg pure and Mg-xAg alloys.

First, in the case of DMEM (a cell culture medium with Mg, Ca, and P content close to that of whole blood) the presence of osteoblasts promotes the formation of MgCO_3 and modifies the Ca/P ratio in the formed amorphous phosphate phase in a way to become closer to that of hydroxyapatite.

Second, the oxidation processes of degradable Mg-based materials can be tailored by appropriate alloying. In particular the addition of silver selectively changes the degradation products to relatively pure MgCO_3 and calcium phosphate phases, which considerably facilitates the activity of osteoblast cells to direct the structure and composition of the formed phosphate phases to the desired apatite type. **This will be further addressed in ongoing studies.**

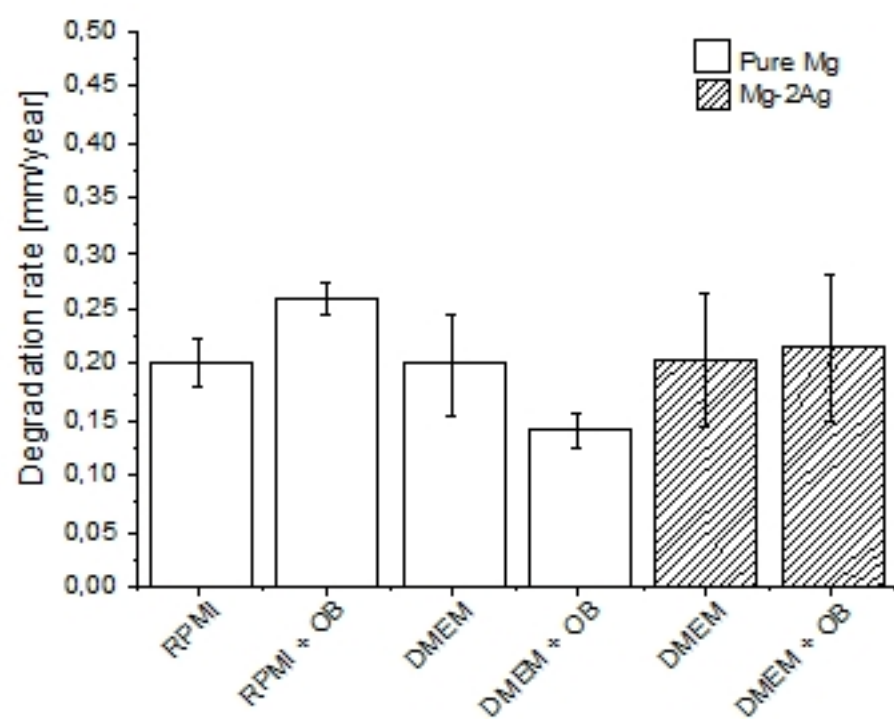
Acknowledgements

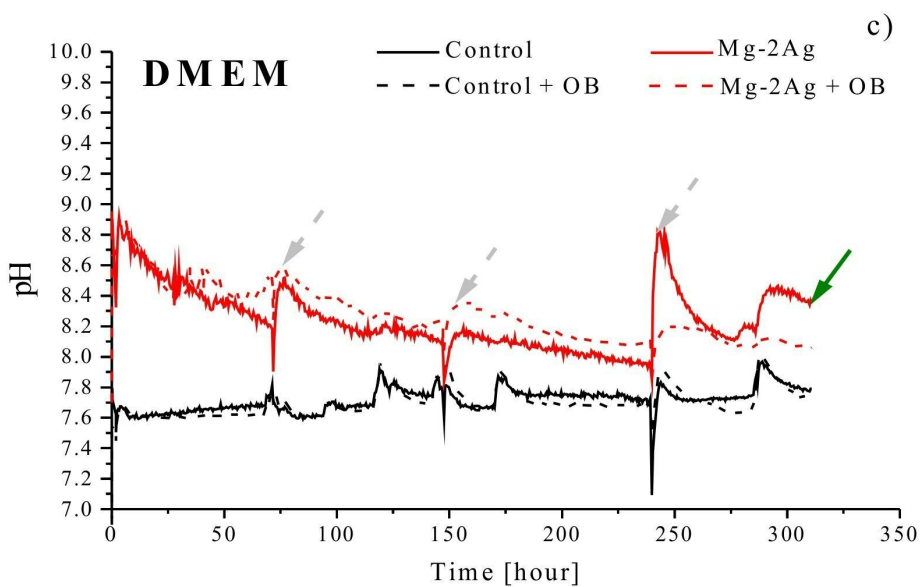
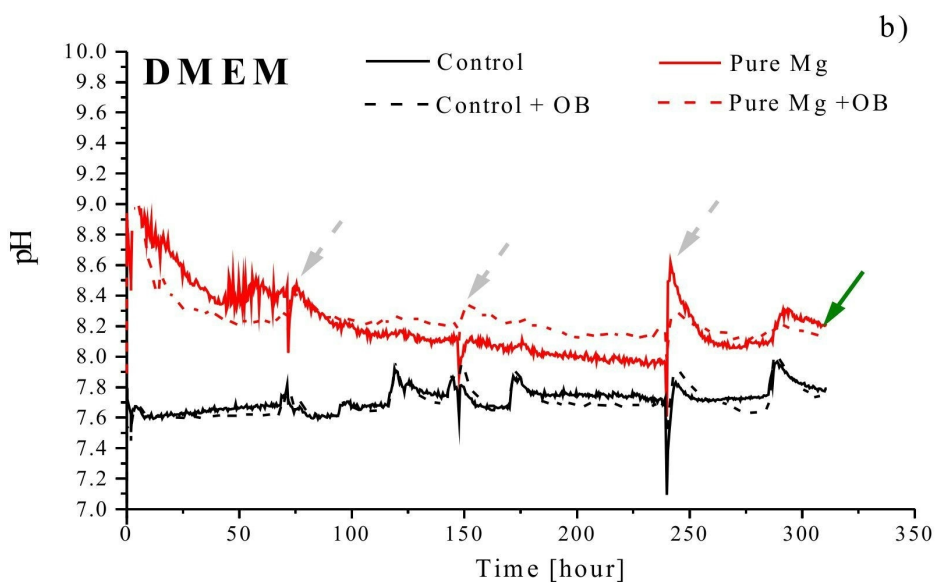
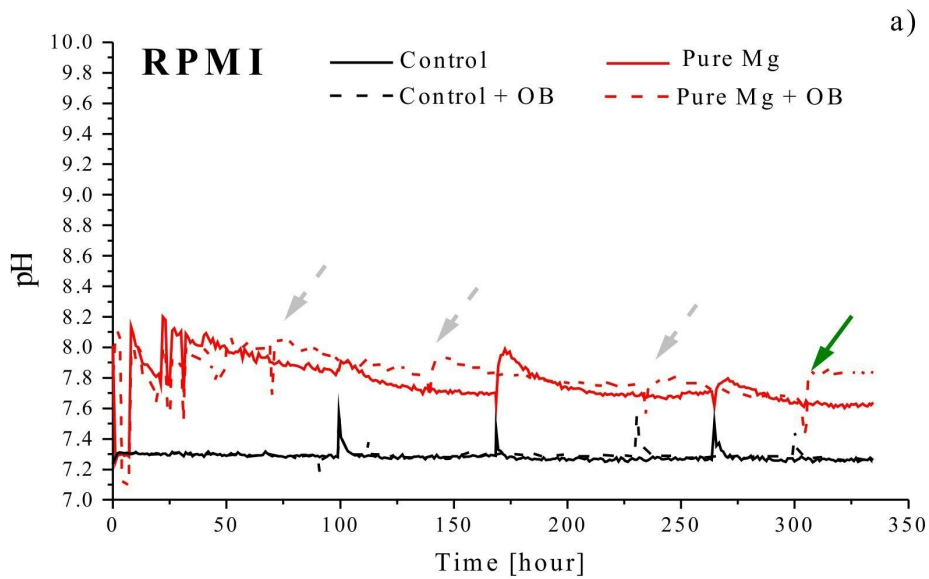
Financial support of this study by Helmholtz Virtuelles Institute VHVI-523 “In vivo studies of biodegradable magnesium based implant materials” (MetBioMat) is gratefully acknowledged. We are also indebted to the Synchrotron Light Source ANKA for provision of instruments at their beamlines and would like to thank Michael Süpflé for assistance in using beamline IR2.

References

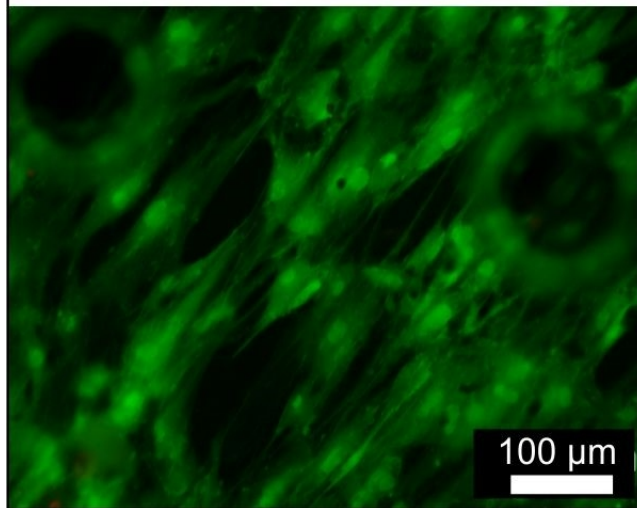
- [1] B.J. Luthringer, F. Feyerabend, R. Willumeit-Romer, *Magnes. Res.*, 27 (2014) 142-154.
- [2] M.P. Staiger, A.M. Pietak, J. Huadmai, G. Dias, *Biomaterials*, 27 (2006) 1728-1734.
- [3] F. Witte, V. Kaese, H. Haferkamp, E. Switzer, A. Meyer-Lindenberg, C.J. Wirth, H. Windhagen, *Biomaterials*, 26 (2005) 3557-3563.
- [4] T. Kraus, S.F. Fischerauer, A.C. Hanzi, P.J. Uggowitzer, J.F. Loffler, A.M. Weinberg, *Acta Biomater*, 8 (2012) 1230-1238.
- [5] H. Liedberg, T. Lundberg, *Br. J. Urol.*, 65 (1990) 379-381.
- [6] J.R. Johnson, P.L. Roberts, R.J. Olsen, K.A. Moyer, W.E. Stamm, *J. Infect. Dis.*, 162 (1990) 1145-1150.
- [7] C.S. Chu, A.T. McManus, B.A. Pruitt, Jr., A.D. Mason, Jr., *J. Trauma*, 28 (1988) 1488-1492.
- [8] D. Tie, F. Feyerabend, W.D. Muller, R. Schade, K. Liefeth, K.U. Kainer, R. Willumeit, *Eur Cell Mater*, 25 (2013) 284-298; discussion 298.
- [9] A. Feng, Y. Han, *Journal of Alloys and Compounds*, 504 (2010) 585-593.
- [10] X.N. Gu, W. Zheng, Y. Cheng, Y.F. Zheng, *Acta Biomater.*, 5 (2009) 2790-2799.
- [11] M.B. Kannan, *Materials Letters*, 64 (2010) 739-742.
- [12] B. Ullmann, J. Reifenrath, J.M. Seitz, D. Bormann, A. Meyer-Lindenberg, *Proc. Inst. Mech. Eng. H*, 227 (2013) 317-326.
- [13] P. Minárik, R. Král, J. Pešička, F. Chmelík, *Journal of Materials Research and Technology*, 4 (2015) 75-78.
- [14] L. Yang, N. Hort, R. Willumeit, F. Feyerabend, *Corrosion Engineering, Science and Technology*, 47 (2012) 335-339.
- [15] R. Willumeit, J. Fischer, F. Feyerabend, N. Hort, U. Bismayer, S. Heidrich, B. Mihailova, *Acta Biomater*, 7 (2011) 2704-2715.
- [16] R. Willumeit, F. Feyerabend, N. Huber, *Acta Biomater.*, 9 (2013) 8722-8729.
- [17] L. Muller, F.A. Muller, *Acta Biomater.*, 2 (2006) 181-189.
- [18] W.D. Mueller, M.F. de Mele, M.L. Nascimento, M. Zeddies, *J. Biomed. Mater. Res. A*, 90 (2009) 487-495.
- [19] N.A. Agha, F. Feyerabend, B. Mihailova, S. Heidrich, U. Bismayer, R. Willumeit-Römer, *Materials Science and Engineering: C*, 58 (2016) 817-825.
- [20] L. Wu, B.J. Luthringer, F. Feyerabend, A.F. Schilling, R. Willumeit, *Acta Biomater.*, 10 (2014) 2843-2854.
- [21] S. Yoshizawa, A. Brown, A. Barchowsky, C. Sfeir, *Acta Biomater.*, 10 (2014) 2834-2842.
- [22] M.M. Belluci, T. Schoenmaker, C. Rossa-Junior, S.R. Orrico, T.J. de Vries, V. Everts, *J. Nutr. Biochem.*, 24 (2013) 1488-1498.
- [23] A. Burmester, R. Willumeit-Romer, F. Feyerabend, *Journal of biomedical materials research. Part B, Applied biomaterials*, (2015).
- [24] N. Ahmad Agha, R. Willumeit-Römer, D. Laipple, B. Luthringer, F. Feyerabend, *PLoS One*, 11 (2016) e0157874.
- [25] F. Feyerabend, H.P. Wendel, B. Mihailova, S. Heidrich, N.A. Agha, U. Bismayer, R. Willumeit-Romer, *Acta Biomater.*, (2015).
- [26] F.M. Mirabella, *Modern Techniques in Applied Molecular Spectroscopy*, John Wiley & Sons, New York, N.Y., 1998.
- [27] O. Mekmene, S. Quillard, T. Rouillon, J.-M. Boulter, M. Piot, F. Gaucheron, *Dairy Science & Technology*, 89 (2009) 301-316.
- [28] R. Willumeit, A. Mohring, F. Feyerabend, *Int. J. Mol. Sci.*, 15 (2014) 7639-7650.

- [29] J. Fischer, D. Pröfrock, N. Hort, R. Willumeit, F. Feyerabend, *Materials Science and Engineering: B*, 176 (2011) 830-834.
- [30] K. Gholivand, Z. Shariatnia, N. Orouzadeh, *Heteroatom Chemistry*, 24 (2013) 404-412.
- [31] S.-Y. Lin, M.-J. Li, W.-T. Cheng, *Spectroscopy*, 21 (2007) 1-30.
- [32] A.L. Boskey, *Journal of Cellular Biochemistry*, 72 (1998) 83-91.
- [33] H.C. Anderson, *Clin Orthop Relat Res*, (1995) 266-280.
- [34] S. Boonrungsiman, E. Gentleman, R. Carzaniga, N.D. Evans, D.W. McComb, A.E. Porter, M.M. Stevens, *Proceedings of the National Academy of Sciences*, 109 (2012) 14170-14175.
- [35] J. Mahamid, B. Aichmayer, E. Shimoni, R. Ziblat, C. Li, S. Siegel, O. Paris, P. Fratzl, S. Weiner, L. Addadi, *Proceedings of the National Academy of Sciences*, 107 (2010) 6316-6321.
- [36] K. Jähn, H. Saito, H. Taipaleenmäki, A. Gasser, N. Hort, F. Feyerabend, H. Schlüter, J.M. Rueger, W. Lehmann, R. Willumeit-Römer, E. Hesse, *Acta Biomaterialia*, 36 (2016) 350-360.
- [37] Y. Zhang, J. Xu, Y.C. Ruan, M.K. Yu, M. O'Laughlin, H. Wise, D. Chen, L. Tian, D. Shi, J. Wang, S. Chen, J.Q. Feng, D.H.K. Chow, X. Xie, L. Zheng, L. Huang, S. Huang, K. Leung, N. Lu, L. Zhao, H. Li, D. Zhao, X. Guo, K. Chan, F. Witte, H.C. Chan, Y. Zheng, L. Qin, *Nat Med*, advance online publication (2016).
- [38] X. Wu, M. Lin, Y. Li, X. Zhao, F. Yan, *Cytotechnology*, 59 (2009) 103-111.
- [39] S. Yuasa, J. Oró, Role of Weak Bases on the Prebiotic Formation of Heterocyclic Compounds, in: J. Oró, S.L. Miller, C. Ponnampereuma, R.S. Young (Eds.) *Cosmochemical Evolution and the Origins of Life: Proceedings of the Fourth International Conference on the Origin of Life and the First Meeting of the International Society for the Study of the Origin of Life*, Barcelona, June 25-28, 1973 Volume II: Contributed Papers, Springer Netherlands, Dordrecht, 1974, pp. 295-299.
- [40] B.V. Parakhonskiy, A. Haase, R. Antolini, *Angewandte Chemie International Edition*, 51 (2012) 1195-1197.
- [41] V. Pipich, M. Balz, S.E. Wolf, W. Tremel, D. Schwahn, *J Am Chem Soc*, 130 (2008) 6879-6892.
- [42] T. Chen, A. Neville, M. Yuan, *Journal of Crystal Growth*, 275 (2005) e1341-e1347.

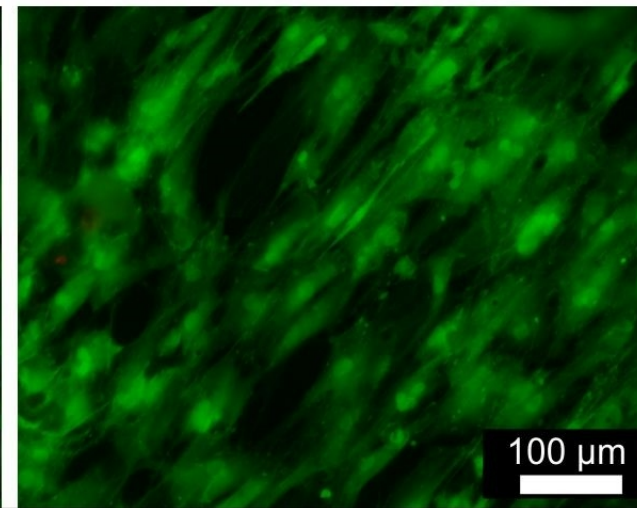
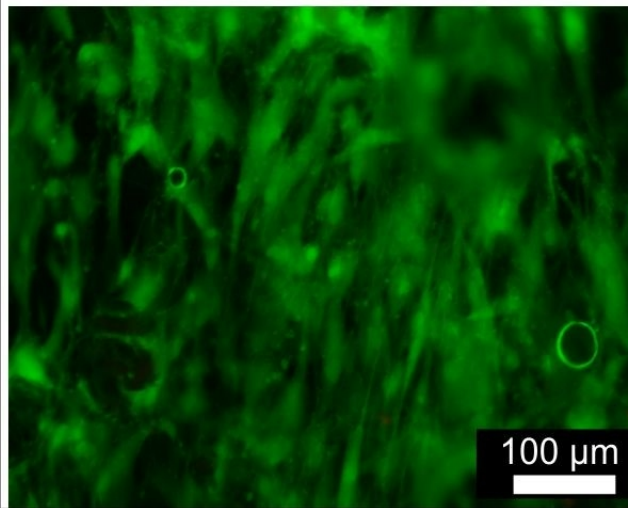


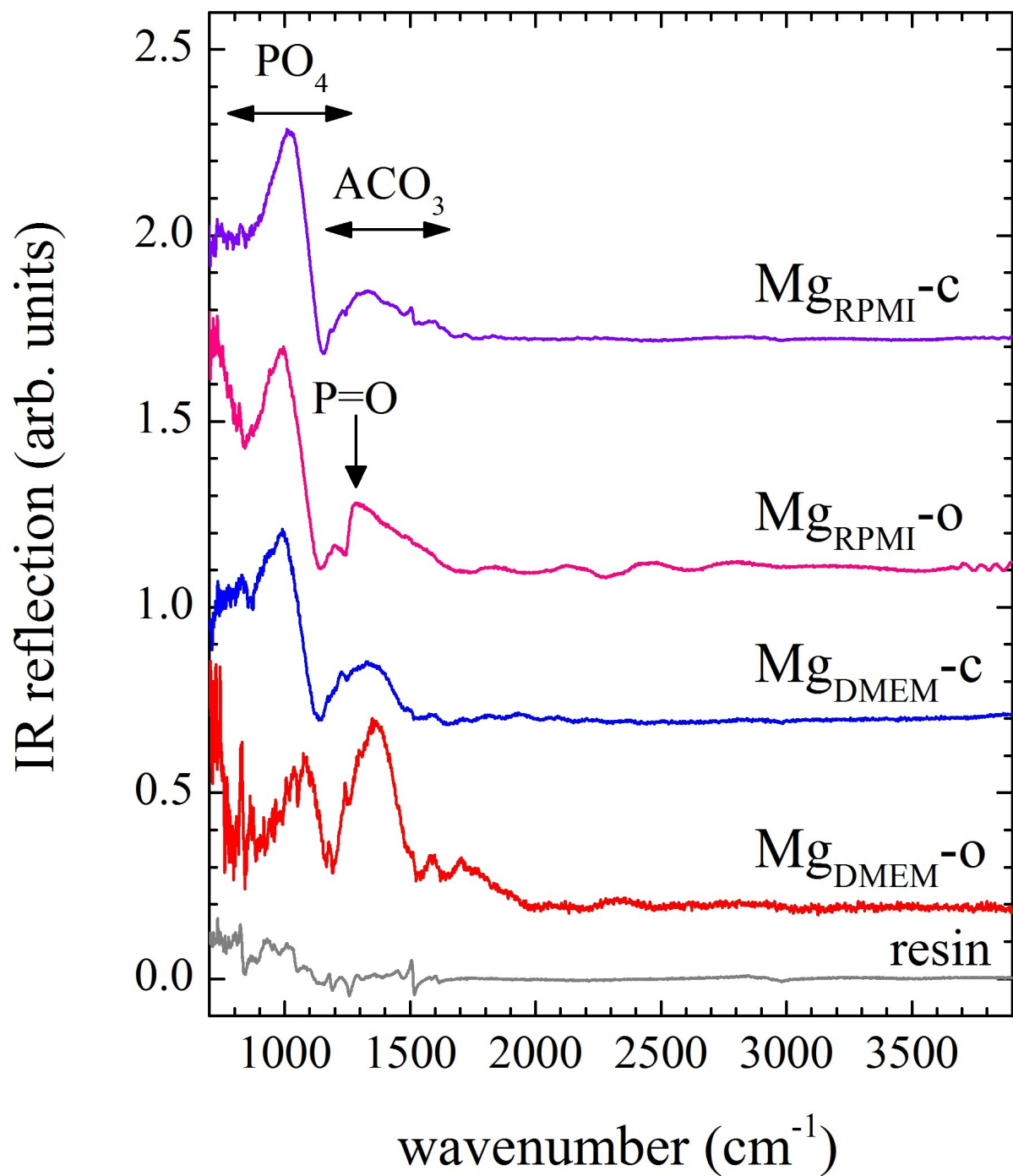


RPMI
Pure Mg

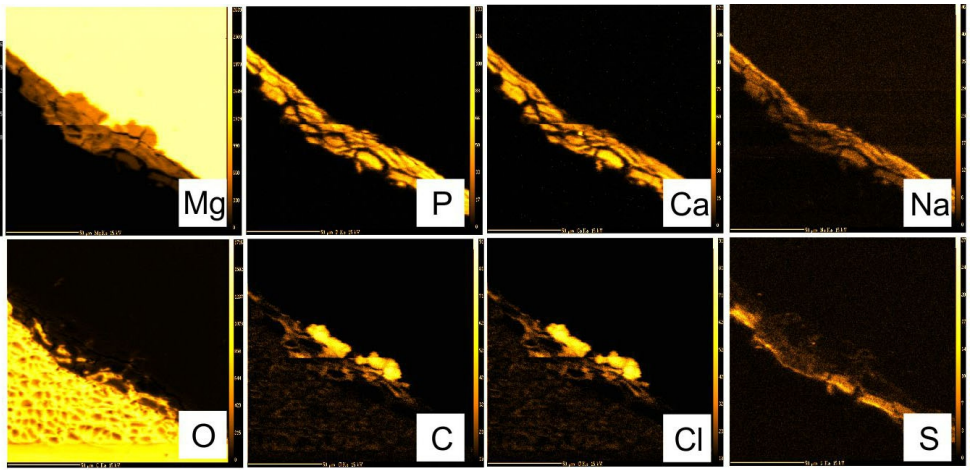
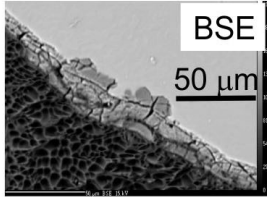


DMEM
Pure Mg Mg-2Ag

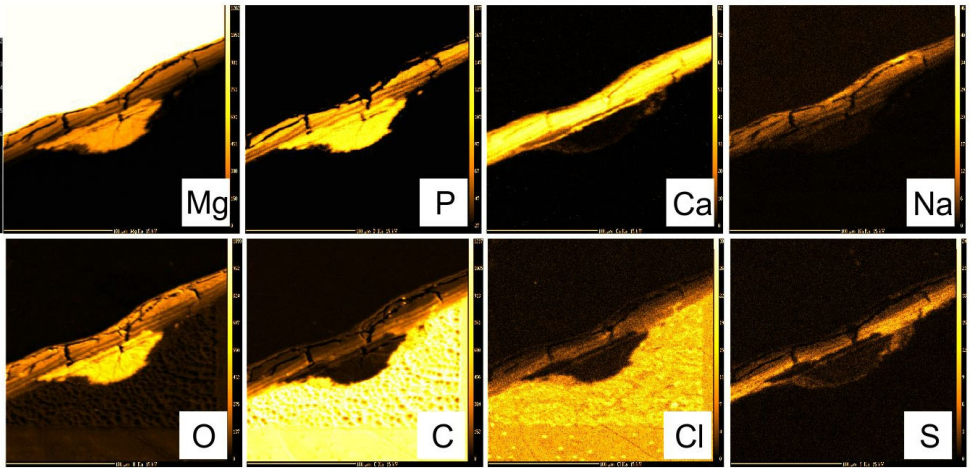
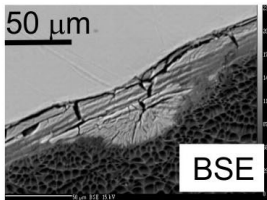




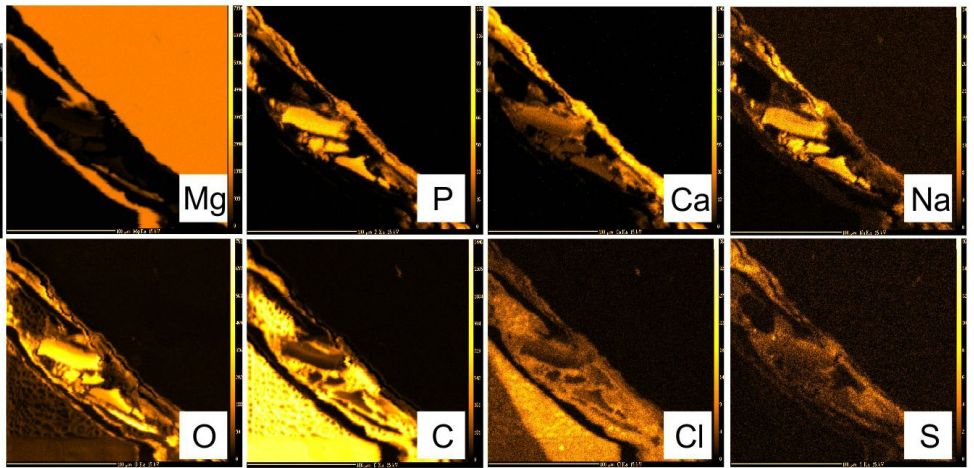
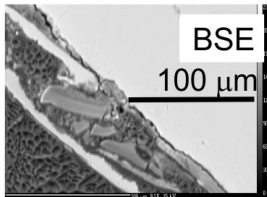
RPMI



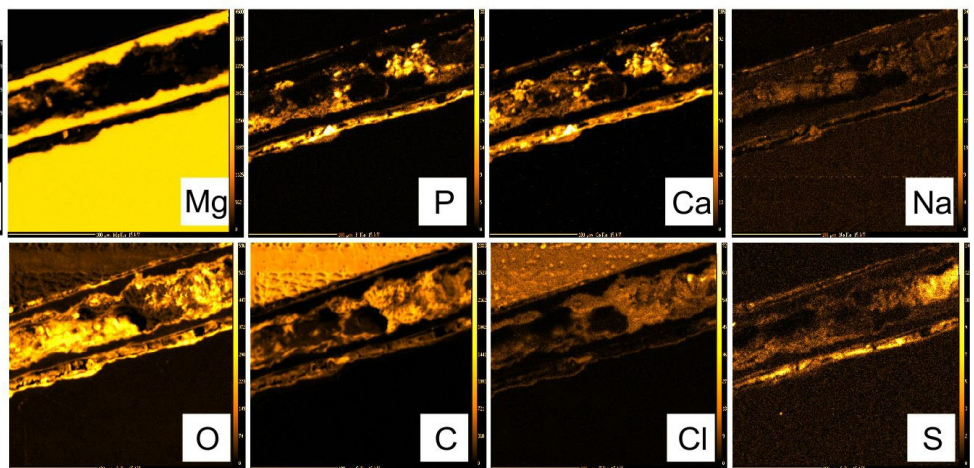
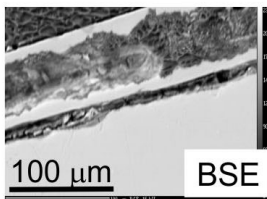
RPMI + OB

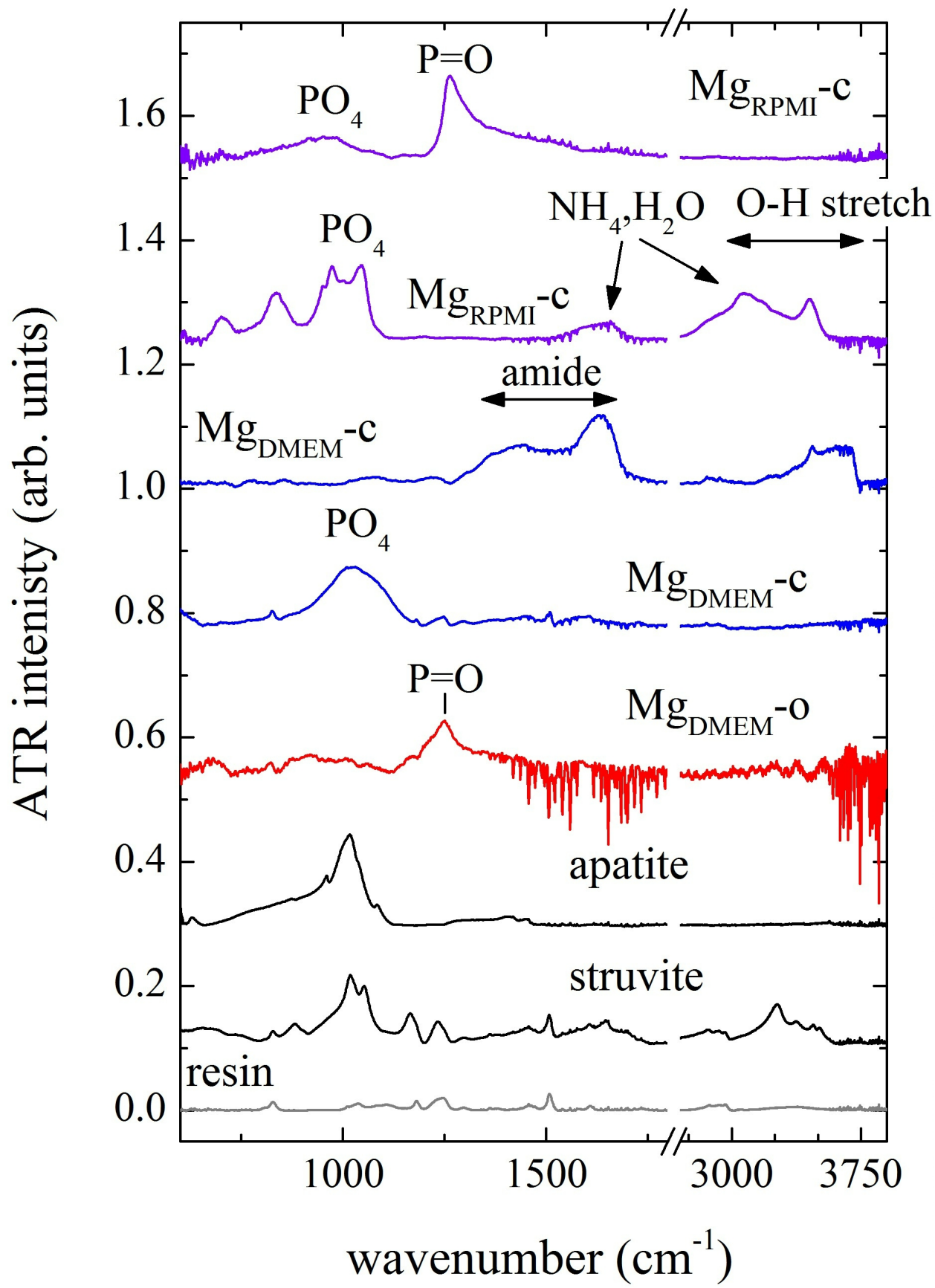


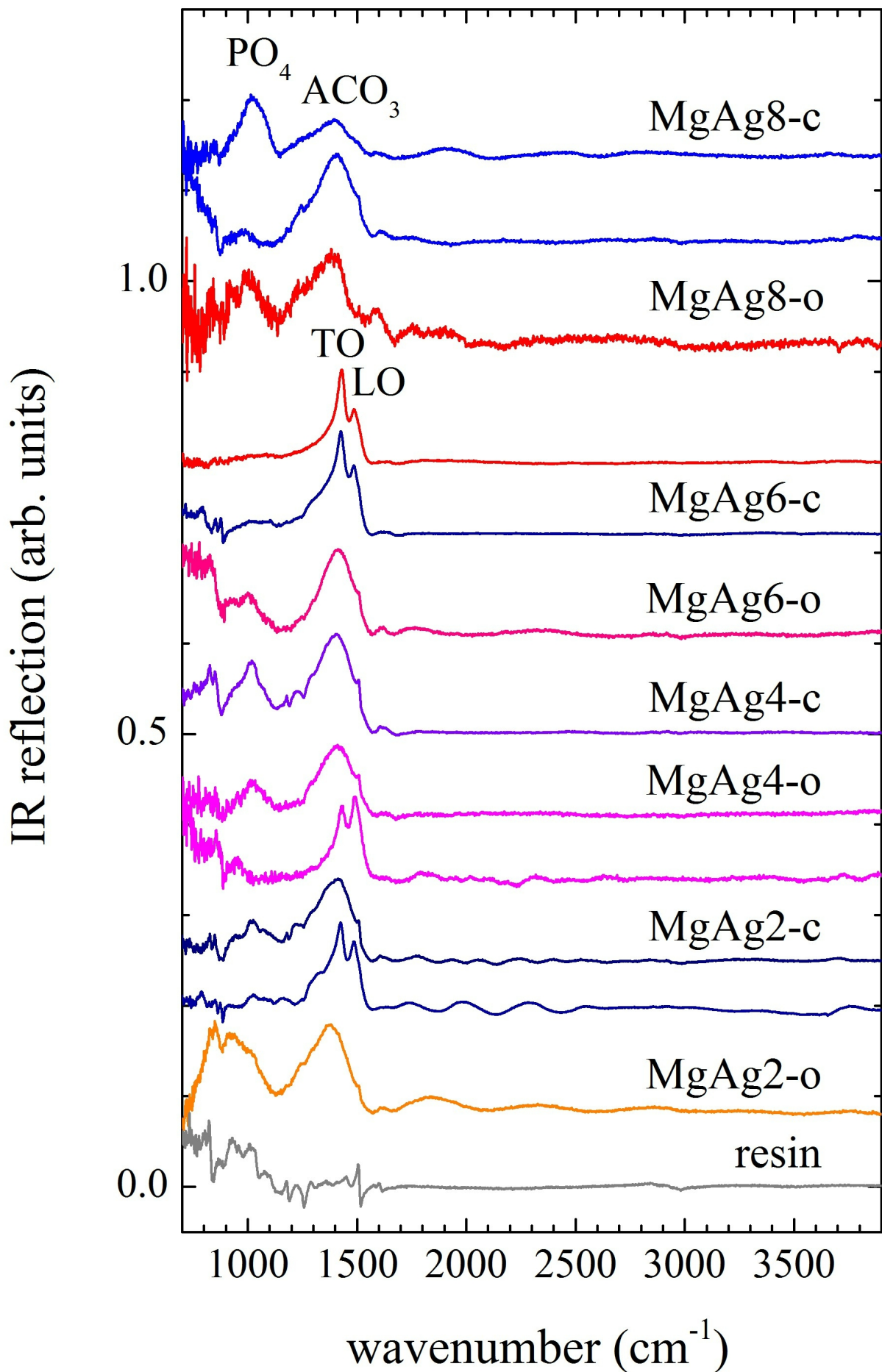
DMEM



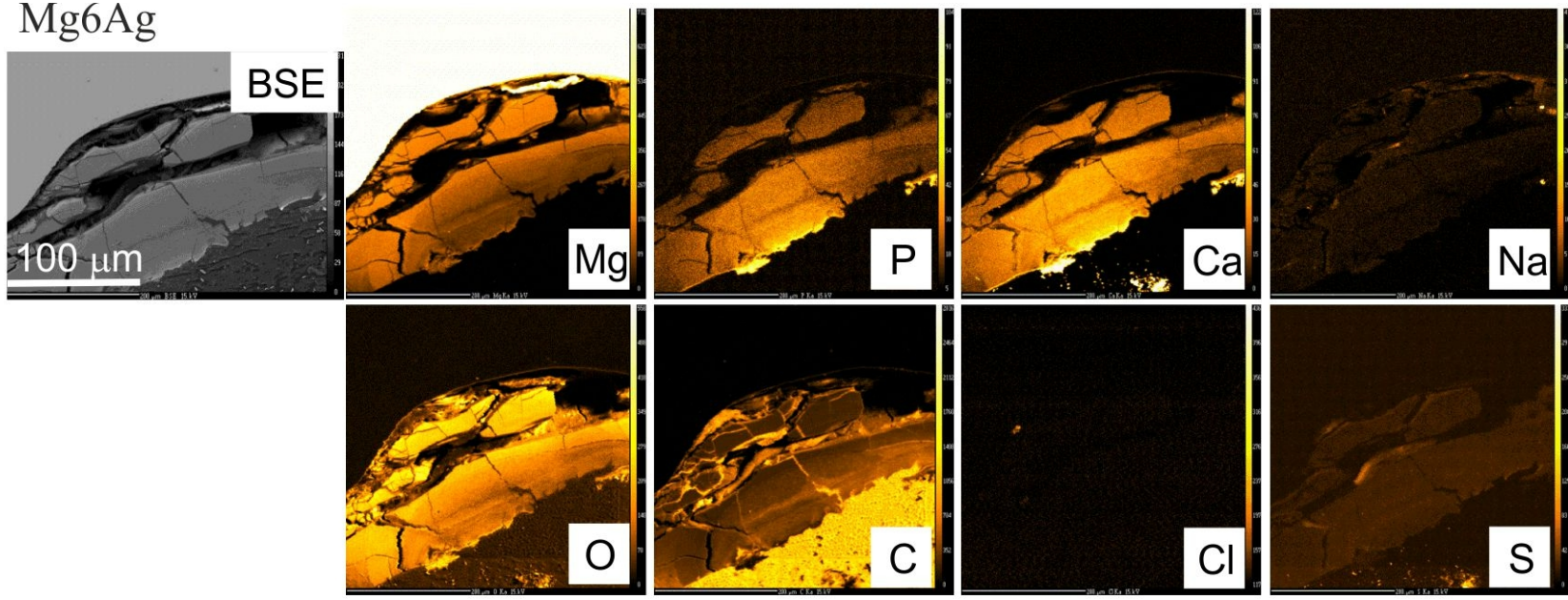
DMEM + OB







Mg6Ag



Mg6Ag+ OB

